

Article

Green Hydrothermal Synthesis of Zinc Oxide Nanoparticles for UV-Light-Induced Photocatalytic Degradation of Ciprofloxacin Antibiotic in an Aqueous Environment

Maha G. Batterjee¹, Arshid Nabi² , Majid Rasool Kamli^{3,4} , Khalid Ahmed Alzahrani¹, Ekram Y. Danish¹  and Maqsood Ahmad Malik^{1,*} 

¹ Chemistry Department, Faculty of Science, King Abdulaziz University, P.O. Box 80203, Jeddah 21589, Saudi Arabia

² Department of Chemistry, University of Malaya, Kuala Lumpur 50603, Malaysia

³ Department of Biological Sciences, Faculty of Sciences, King Abdulaziz University, P.O. Box 80203, Jeddah 21589, Saudi Arabia

⁴ Center of Excellence in Bionanoscience Research, King Abdulaziz University, P.O. Box 80203, Jeddah 21589, Saudi Arabia

* Correspondence: mamalik@kau.edu.sa or maqsoodchem@gmail.com

Abstract: The design and development of new cost-effective, clean, and efficient synthesis procedures for the synthesis of nanoparticles have recently become an intriguing research topic with broad implications. This study aimed to develop an eco-friendly biogenic method that uses minimum nontoxic chemicals to yield ZnO nanoparticles with enhanced capabilities for degradation of pharmaceutical by-products. The present study used black dried lemon peel aqueous extract as a biological stabilizing agent to prepare pure and stable zinc oxide nanoparticles (LP-ZnO NPs). The surface morphology, elemental composition, crystalline properties, size, optical properties, the role of functional groups in stabilization, capping, and the thermal stability of LP-ZnO NPs were investigated using scanning electron microscopy equipped with energy dispersive X-ray (SEM-EDX), X-ray diffraction (XRD), UV-visible diffuse reflectance spectroscopy (UV-DRS), PL, Fourier transform infrared (FTIR), Raman spectra, and thermogravimetric (TGA) analyses. Multiphoton resonances were observed in LP-ZnO NPs along the crystalline structure as per Raman analysis. The developed LP-ZnO NPs were thermally stable at an annealing temperature of 500 °C with a weight loss of 53%. Photodegradation of antibiotic ciprofloxacin was observed in the presence of UV light via LP-ZnO NPs (serving as photocatalyst). In addition, in optimal reaction media, the biogenic LP-ZnO NPs retained improved photocatalytic performance toward ciprofloxacin. Meanwhile, in the photodegradation process of CPI molecules via ZnO as a photocatalyst, the optimum catalytic dose, concentration of CIP molecules, and pH were attained at 10 mg, 2×10^{-5} M, and pH 8, respectively. The aim of this research work was to develop a simple, affordable photocatalytic technique for the photodegradation of antibiotics in aqueous media. The photocatalytic process was performed under different experimental conditions, including varying catalytic doses, ciprofloxacin concentrations, and pH of the reaction mixture.

Keywords: green synthesis; zinc oxide; photocatalysis; antibiotics



Citation: Batterjee, M.G.; Nabi, A.; Kamli, M.R.; Alzahrani, K.A.; Danish, E.Y.; Malik, M.A. Green Hydrothermal Synthesis of Zinc Oxide Nanoparticles for UV-Light-Induced Photocatalytic Degradation of Ciprofloxacin Antibiotic in an Aqueous Environment. *Catalysts* **2022**, *12*, 1347. <https://doi.org/10.3390/catal12111347>

Academic Editor: Ewa Kowalska

Received: 18 September 2022

Accepted: 27 October 2022

Published: 2 November 2022

Publisher's Note: MDPI stays neutral with regard to jurisdictional claims in published maps and institutional affiliations.



Copyright: © 2022 by the authors. Licensee MDPI, Basel, Switzerland. This article is an open access article distributed under the terms and conditions of the Creative Commons Attribution (CC BY) license (<https://creativecommons.org/licenses/by/4.0/>).

1. Introduction

Nature serves as a biolaboratory that has never-ending replenishment of supplies for biogenic synthesis. In contrast to the typical chemical approach, important biomaterials are available to utilize the challenging and exceptional biocompatible yield of nanomaterials. Green synthesis has several advantages over traditional conventional methods. Nanoscale particles (NPs) have an increased surface area to volume ratio, enhancing their ability to react with catalysts, and possess nonlinear photosensitive, chemical stability, and thermal properties [1,2]. Biomedical uses of nanomaterials have been hailed as the most significant

medical breakthroughs in the history of humankind [3,4]. Due to their large surface ratio, metallic nanoparticles exhibit distinct physical and chemical properties compared to their bulk counterparts [5]. The biocompatible, cost-effective, and safe technique of synthesizing nanoparticles (NPs) from biomass, including plant extracts, bacteria, fungi, and algae, using green technologies is given preference nowadays by academics and industrial researchers [6–9].

Additionally, the introduction of green and eco-friendly synthesis of NPs has found wide applications in food, space, consumer healthcare, pharmaceutical and cosmetic industries. Such biogenic NPs were recently cited as significant functional entities that play a role in the prevention of illness and in combating healthcare-related infections [10–12]. Inorganic metal oxides, such as TiO₂, CuO, and ZnO, have been produced and employed in recent investigations. ZnO NPs are the most interesting of these metal oxides as they are inexpensive to produce sufficient yield using green methods. Zinc oxide (ZnO), an n-type semiconducting metal oxide with a wide range of uses in electronics, optics, and healthcare systems, maintains its innate reducing nature. ZnO has been classified as a GRAS (generally regarded as safe) metal oxide by the US Food and Drug Administration [13–15]. Plants, algae, and microbes are attractive candidates for nanoparticle manufacturing because they contain bioactive chemicals [16–19].

The pharmaceutical industry is one of the most significant industries. The general quality of life has increased due to the widespread availability of healthcare items, including antibiotics, analgesics, anti-inflammatories, hypnotics, etc. However, large amounts of these medicinal compounds are intentionally and unintentionally released into the environment. As a result, these pharmaceutical substances are present in various environmental components, including soil, water surfaces, and even in drinking water. Therefore, these pharmaceutical compounds are regularly found in natural and wastewater systems [20–23].

The by-products released from the pharmaceutical industry have a direct impact on aquatic environments. Therefore, they are a cause for concern worldwide. Furthermore, they can have long-term effects on aquatic organisms even at low concentrations, and an increased number of infectious pathogens resistant to antibiotics are found in wastewater [24–26]. In general, some antibiotics can be eliminated from water bodies by different techniques, such as adsorption, nanofiltration, coagulation, electrolysis, and biodegradation [27–34]. However, high operational costs and poor removal efficiency are the main obstacles to their widespread use. Advanced oxidation processes (AOPs) have demonstrated the capacity to decompose antibiotics and transform them into minute, nontoxic, and biodegradable molecules, thereby reducing the adverse effects of antibiotics on microorganisms and the environment [27]. Moreover, to remove organic molecules in particular antibiotics, AOPs have been used as powerful oxidizing agents after the formation of chloride (Cl), hydroxyl radicals (\bullet OH), ozone (O₃), and superoxide radicals (\bullet O₂) in photocatalytic degradation [27,34–36].

ZnO possesses a special place among various heterogeneous semiconductor photocatalysts due to its inherent properties, such as long-term stability, nontoxicity, low-cost synthesis, easy recovery by filtration and centrifugation methods, wide bandgap ($E_{bg} = 3.2$ eV), and several other excellent properties [37,38]. In addition, ZnO possesses an excellent oxidizing capacity, has enhanced photosensitivity as a catalyst, and is eco-friendly and safe for nature [39]. These attributes collectively make biogenic LP-ZnO a suitable photocatalyst for the degradation of ciprofloxacin as a pharmaceutical pollutant and provide an alternative solution to this environmental pollution problem. In the present study, LP-ZnO NPs were synthesized by a simple, green synthesis method. In this method, lemon peel with various phytochemical compositions served as the reducing and capping agents in biosynthesis of LP-ZnO NPs. The photocatalytic activity of the prepared LP-ZnO NPs was evaluated for the degradation of ciprofloxacin as a model antibiotic compound under UV light illumination.

2. Experimental Section

2.1. Chemicals

Zinc nitrate hexahydrate $\text{Zn}(\text{NO}_3)_2 \cdot 6\text{H}_2\text{O}$ as a metal precursor for the preparation of ZnO NPs was acquired from Sigma-Aldrich. Ciprofloxacin ($\text{C}_{17}\text{H}_{18}\text{FN}_3\text{O}_3$), a common fluoroquinolone antibiotic, was purchased from Sigma-Aldrich. Black dried lemons, commonly available from the local market in Jeddah, Saudi Arabia, were utilized as bioreducing agents. All the solutions and plant extracts were prepared in deionized water.

2.2. Preparation of Aqueous Lemon Peel Extract and LP-ZnO NPs

Black dried lemons were washed and dried before peeling as thinly as possible to collect the essence. The peel was then dried for 12 h in a food dehydrator before being powdered into a medium-fine powder. After that, 5 g of the powder was poured into each of the 250 mL beakers with 100 mL deionized water and swirled for 3 h. Next, each mixture was macerated before being immersed in an 80 °C water bath for 2 h. Finally, the extracts were filtered and stored in an argon environment for subsequent use. LP-ZnO NPs were prepared by a facile, low-cost, phytochemical mediated green hydrothermal synthesis approach using an aqueous extract of dried lemon peel powder. In a typical preparation method, 50 mL of 0.1 M aqueous solution of zinc nitrate was mixed with 50 mL of aqueous lemon peel extract under continuous stirring for 30 min at 50 °C. Next, the reaction mixture was transferred to a Teflon-lined autoclave and kept for 18 h at 180 °C in an oven. The autoclave was cooled down to room temperature, and the acquired solid precipitate was washed with deionized water and ethanol and centrifuged at 4000 rpm for 10 min. The as-prepared phytochemical capped metal oxide nanoparticles were further purified by washing several times with deionized water followed by ethanol to remove all impurities from the surface of the synthesized material. The solid material was dried at 120 °C for 12 h in an oven and finally transferred to the silica crucible for calcination in a muffle furnace at 500 °C for 4 h, leading to the formation of stable LP-ZnO NPs. After hydrothermal treatment followed by calcination, pure and crystalline ZnO nanoparticles were formed [40]. Figure 1 depicts the complete synthesis procedure of the ZnO nanoparticles using aqueous lemon peel extract.

The phytochemical mediated synthesis mechanism of metal oxide nanoparticles is still an unknown process and needs extensive investigation [41]. Dried lemon peel extract is rich in flavonoids, phenols, alkaloids, proteins, carbohydrates, amino acids, tannins, steroids, and cardiac glycosides. These phytochemicals present in the aqueous extract are mainly responsible for the formation of metal and metal oxide nanoparticles due to their reducing and stabilizing/capping properties [7]. Based on previous studies [42], we proposed a possible mechanism by which the phytochemicals of lemon peel extract acts as reducing and stabilizing agents [41]. The possible synthetic mechanism of LP-ZnO NP formation is given in Figure 2. The phytochemicals of dried lemon peel extract first reduce the metallic Zn ions. Then, the oxygen-containing functional groups of the phytochemicals bind to the reduced metal ions, forming an organic coat to create metal oxides [42]. Additionally, phytochemicals help in the stabilizing and growth process of metal oxide nanoparticles to prevent aggregation/agglomeration between particles. For metal oxide nanoparticle formation, atmospheric oxygen or oxygen from degrading phytochemicals of dried lemon peel bind to the zinc metal ion before growth and stabilization of the synthesized material.

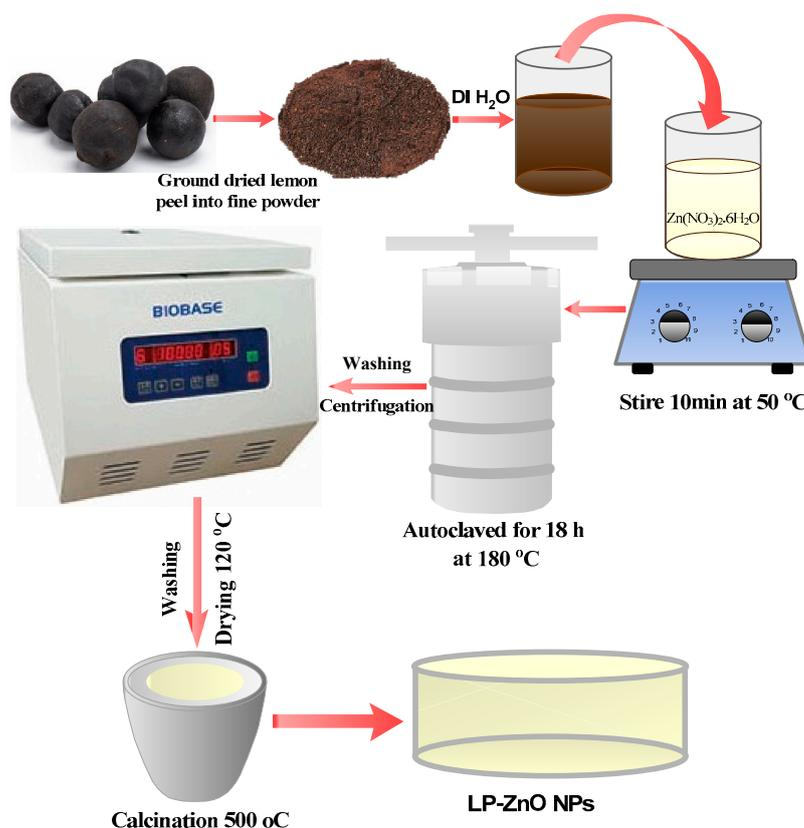


Figure 1. Schematic representation of the preparation of LP-ZnO NPs.

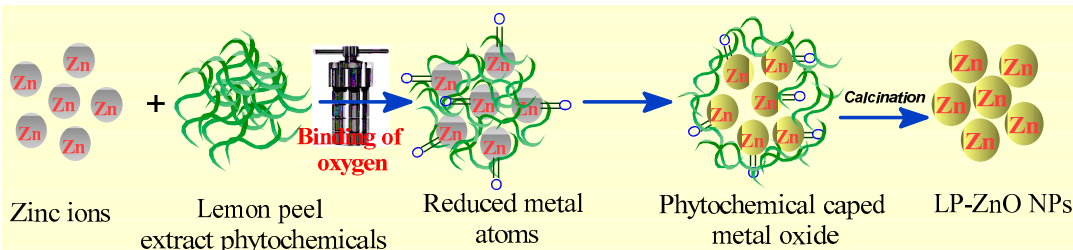


Figure 2. Possible mechanism of LP-ZnO NP formation using lemon peel aqueous extract.

2.3. Characterization

The as-prepared LP-ZnO NPs were further characterized by different techniques to investigate their surface morphology, thermal stability, and physicochemical structural properties. Initially, the as-synthesized LP-ZnO NPs were characterized by X-ray diffraction (XRD) for phase identification and purification using a Bruker D8 Advance diffractometer with Cu K α radiation ($\lambda = 1.5418 \text{ \AA}$) generated at 40 kV and at 30 mA current. Ultraviolet-diffused reflectance (UV-DRS) spectroscopy (Shimadzu, Japan) was used to obtain the absorption spectra of the nanoparticles over a range of 200–900 nm. FTIR analysis in the range of 4000–400 cm^{-1} was performed on Bruker ATRII to confirm the active role of functional groups in stabilization/capping and reduction during LP-ZnO NP formation. A scanning electron microscope (SEM) equipped with energy-dispersive X-ray spectroscopy (EDX) was used to analyze surface morphology and the elemental composition of prepared LP-ZnO NPs. For photoluminescence (PL) spectroscopy, a fluorescence spectrophotometer (FLS920T) with a xenon lamp was utilized, and the PL spectra were acquired at room temperature in an ambient atmosphere. A Bruker MultiRAM Raman spectrometer was used to record Raman spectra at ambient temperature. A Netzsch thermogravimetric analyzer (TGA) type SAT 449 F3 was used to perform TGA.

2.4. Photocatalytic Dye Degradation

The photocatalytic properties of LP-ZnO NPs toward the degradation of ciprofloxacin as a model pharmaceutical effluent were studied. The photocatalytic degradation was carried out in a TECHINSTRO photochemical reactor under UV light irradiation. The photocatalytic reaction chamber consisted of a double-walled chamber with a cooling jacket made of quartz and an outer coat of borosilicate. A medium-pressure mercury lamp with a 365 nm wavelength range was used as a light source to generate a sufficient photon source for photocatalytic reaction. In a typical photocatalytic reaction, 5 mg of LP-ZnO NPs was dispersed in 100 mL (1.0×10^{-4} M) of ciprofloxacin aqueous solution under constant stirring in dark conditions. It took 30 min to achieve adsorption/desorption equilibrium. After UV light irradiation, the photocatalytic behavior of LP-ZnO NPs was studied using a UV-visible spectrophotometer by taking a small aliquot of the reaction mixture after fixed time intervals. The photocatalytic degradation efficiency of LP-ZnO NPs against ciprofloxacin was measured using degradation efficiency = $(C_0 - C_t)/C_0 \times 100$, and the rate constant of the reaction was calculated using the Langmuir-Hinshelwood model $\ln C_0/C_t = k_{app} t$, where C_0 is the ciprofloxacin concentration before UV light irradiation, C_t is the ciprofloxacin concentration after UV light irradiation at fixed time intervals, k_{app} refers to the pseudo-first-order rate constant, and t is the UV light irradiation time. The reusability of experiments with LP-ZnO NPs against ciprofloxacin degradation was measured for five consecutive cycles. To detect the active species responsible for ciprofloxacin degradation during the photocatalytic reaction, superoxide radicals ($\bullet O_2^-$), hydroxyl radicals ($\bullet OH$), and holes (h^+) were investigated by adding 1.0 mM benzoquinone (BQ, a quencher of $\bullet O_2^-$), 1.0 mM isopropyl alcohol (IPA, a quencher of $\bullet OH$), or 1.0 mM ethylene-diaminetetraacetate (EDTA, a quencher of h^+) to a reaction mixture at optimum experimental conditions (10 mg LP-ZnO NPs + 2×10^{-5} M ciprofloxacin aqueous solution at pH = 8). The absorbance of the reaction mixture was measured under UV light irradiation, and the degradation percentage was observed.

3. Results and Discussion

3.1. Morphological and Structural Analysis of LP-ZnO NPs

To investigate the formation of LP-ZnO NPs stabilized by lemon peel extract, the samples were analyzed by XRD analysis. The XRD patterns of biosynthesized LP-ZnO NPs are shown in Figure 3, where the narrow and sharp diffraction peaks indicate the formation of stable and highly pure crystalline material. The XRD patterns showed distinguishable peaks at 2θ values of 31.86° , 34.48° , 36.41° , 47.65° , 56.68° , 62.96° , 66.41° , 67.93° , 69.10° , 72.55° , and 77.10° , which were assigned to (100), (002), (101), (102), (110), (103), (200), (112), (201), (004), and (202) lattice planes, respectively, corresponding to the hexagonal wurtzite structure according to the JCPDS card No.00-036-1451 [43,44]. The average particle size of the LP-ZnO NPs was measured by recording the full width at half maxima (FWHM) of the diffraction peaks using the Debye-Scherrer equation $D = k \lambda / \beta \cos\theta$, where k is the particle shape factor that depends on the shape of the particle. Its value is 0.90 for hexagonal particles, λ is the wavelength of Cu K α radiation (0.15406 nm), β is the full width at half maximum (FWHM) of the selected diffraction peaks in radians, and θ represents the Bragg diffraction angle in degrees obtained from 2θ of the same plane [38]. The average crystalline size of the as-synthesized LP-ZnO NPs was 20 nm.

UV-visible DRS spectrometer analysis was performed to study the optical properties and bandgap energy using the Tauc plot, as shown in Figure 4a,b. After electron transfer from the valence band to the conduction band, the DRS spectrum exhibited a well-defined distinctive absorption peak at ca. 362 nm associated with the intrinsic bandgap absorption of LP-ZnO NPs [45]. In addition, LP-ZnO NP absorption spectra indicated a restricted dispersion of nanoparticles [46]. Unlike metals with integral electron levels, semiconductors, including LP-ZnO NPs, possess definite bandgap energy. In this regard, we calculated optical bandgap energy for LP-ZnO NPs, which were about 3.20 eV, as depicted in Figure 4b. The observed lower numerical values of bandgap energy showed that the as-synthesized LP-

ZnO NPs had inherited both excellent electronic transaction capability and photocatalytic capability.

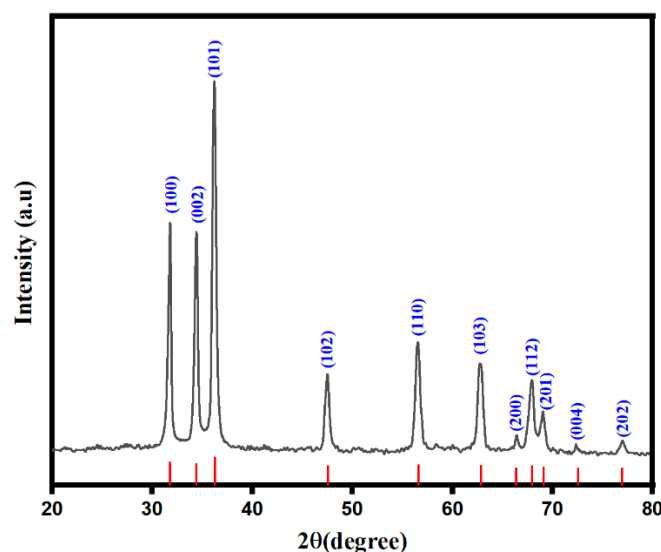


Figure 3. XRD pattern of LP-ZnO NPs.

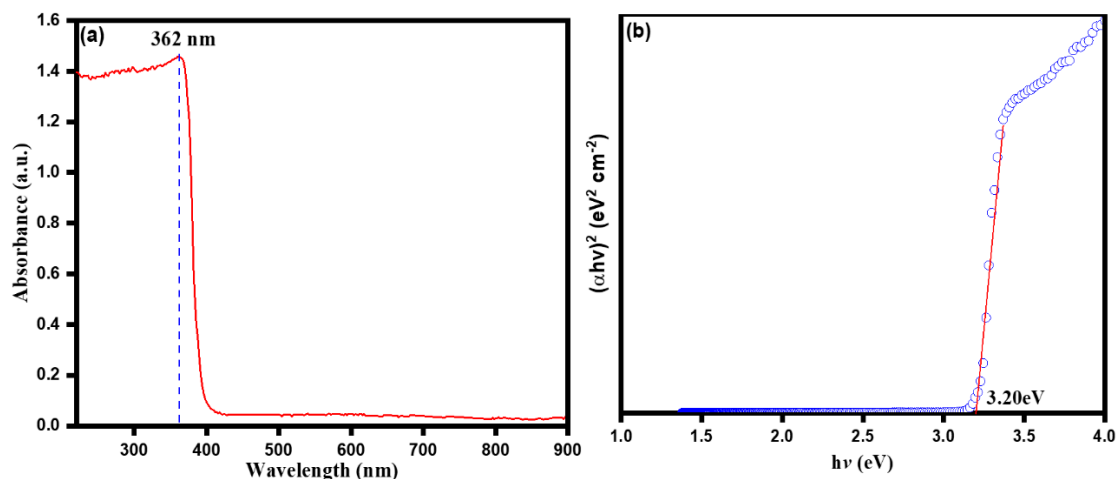


Figure 4. UV-visible DRS spectra (a) and bandgap energy (b) plot of LP-ZnO NPs.

The photoluminescence (PL) spectra of LP-ZnO NPs were recorded at room temperature at an excitation wavelength of 325 nm to study the impact of the as-prepared material on the recombination likelihood of photoinduced charge carriers, the efficiency of charge carrier trapping and recombination kinetics, and information regarding the presence of surface states. The photoluminescence spectra, as shown in Figure 5, exhibited five emission peaks centered at 400, 420, 450, 468, 482, 492, and 516 nm. ZnO showed two PL emission bands: one in the UV region (around 370–400 nm), such as at 400 nm, and one in the visible region of broadband (400–600 nm), such as the observed visible violet peak intensities of 413, 420, and 450 nm; visible blue intensity at 468 nm; and visible green intensities at 469, 497, and 513 nm. The width of such peak intensities in their corresponding band is related to the material's morphology. Strong and sharp UV emission bands are usually observed in nanorods and nanotubes instead of relatively weak and broader visible emissions [47,48]. However, quantum dots of spherical morphology with a weak UV emission band are observed rather than a widespread broad visible emission band [49,50]. In the present study, the relative sharp intensity in the UV region and comparatively broader and low-intensity peaks in the entire visible band indicated the spherical or nearly spherical morphology

of LP-ZnO NPs with rod-like patterns, as shown in the SEM images, which are further described in detail below.

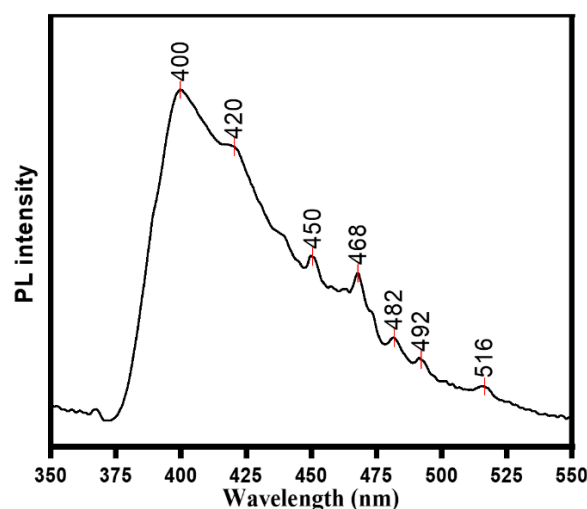


Figure 5. The photoluminescence (PL) spectra of LP-ZnO NPs.

The phytochemical composition of dry lemon peel primarily includes cellulose, hemicellulose, pectin chain, polyphenols, flavonoids as flavones-O-glycosides, flavones-C-glycosides, flavanols, and flavanones. The inner part of dry lemon contains a significant amount of citric acid [51,52]. LP-ZnO NPs were prepared and stabilized by these phytochemical moieties. LP-ZnO NP stabilized surface was characterized by FTIR to check the presence of various functional groups on the surface of the nanoparticles. Figure 6a presents the FTIR spectra of lemon peel extract with the presence of phytochemical compounds, such as cellulose, hemicellulose, polyphenols, and biomolecules. The observed valence vibrations of O-H bonds were attributed to 3600 and 3258.8 cm^{-1} due to free and bound moisture and the presence of hydroxyl groups in cellulose, hemicellulose, and pectin. Valence vibrations of C-H bonds were obtained in the range of 2700 – 2900 cm^{-1} , which were attributed to saturated carbon aromatic rings and vibration bonds in the $-\text{CH}_2-$ groups. Vibrational bands in the range of 2000 – 2400 and 1550 – 1650 cm^{-1} referred to the presence of primary amine $-\text{N-H}$ bond vibration of flavonoids. Valence vibrations of C=O bonds in different functional groups (ester, ketonic, etc.) were observed at 1752.0 cm^{-1} . However, in the case of stabilized ZnO nanoparticles, this band was not obtained, which showed that the Zn^{2+} ions were reduced and stabilized by flavonoids and pectin biomolecules. The broadband in Figure 6a,b at 1250 – 1400 cm^{-1} was attributed to the deformation vibrations of C-H and $-\text{O-H}$ bonds in hexagonal saturated rings and the terminal group $-\text{CH}_2\text{OH}$. Sharp band in the range of 1015 – 1095 cm^{-1} was attributed to the valence vibrations of C-C and C-O bonds in hexagonal saturated rings as well as C-O in the methoxy groups (pectin). It is worth mentioning here that the observed peaks in Figure 6a, such as 1371 and 1303 cm^{-1} , were assigned to acidic hydrogen groups ($-\text{OH}$) and O-H deformation along the C-C stretching vibration associated with phytochemicals of aromatic rings [53]. Meanwhile, the shifting of such intensity peaks was observed in LP-ZnO NPs (Figure 6b) due to the complex split of stretching vibration of $-\text{OH}$. The observed peak at comparatively lower wavenumbers, i.e., between 1020 – 1300 cm^{-1} , such as at 1295 cm^{-1} , was due to the presence of new C-O stretching vibrations [54]. Deformation vibrations in hexagonal saturated rings of pectin were observed in the extract at 854.9 and 897.2 cm^{-1} . Mixed broader vibrations were observed due to the hexagonal saturated rings and deformation vibrations in the methoxy groups. In Figure 6a, sharp bands at 490 – 625 cm^{-1} , such as at 541.7 and 623.5 cm^{-1} , were attributed to the presence of C-alkyl chloride and hexagonal phase of ZnO NPs [55,56]. However, related halogen stretching vibrations shifted to lower wavenumber at 485.3 cm^{-1} , determining the presence of stabilized LP-ZnO nanoparticles [57,58].

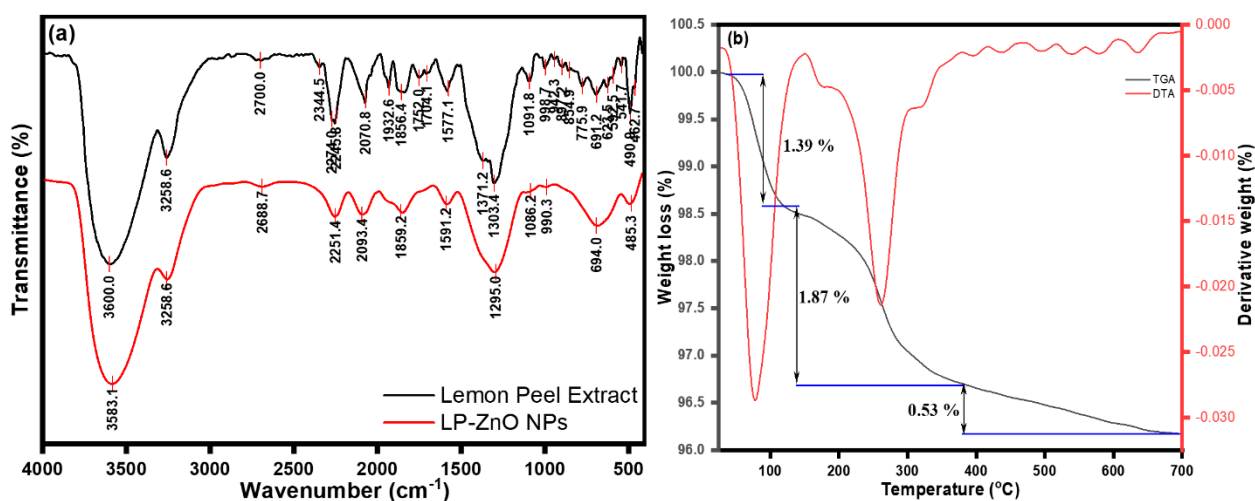


Figure 6. (a) FTIR spectra of lemon peel extract and LP-ZnO NPs and (b) TGA-DTA plot of LP-ZnO NPs.

In a controlled environment, the weight change of a substance in response to temperature is measured by TGA. Information on the physical properties of LP-ZnO NPs and the components on their surface can be gathered from their thermal stability. Figure 6b shows the TGA spectra obtained in a nitrogen atmosphere with a heating rate of 10 °C/min between 0 and 700 °C. The results indicated that a minor weight loss of 1.39 and 1.87% of calcined LP-ZnO NPs at 500 °C occurred in two steps in the temperature range of 45–120 and 120–390 °C, respectively. The DTA analysis revealed that the complex lost 1.39% of its weight at around 100 °C due to the desorption and removal of surface-adsorbed solvents. The second weight loss of 1.87% up to 390 °C indicated the removal of the remaining volatile molecules from the surface of LP-ZnO NPs. In addition, the exothermic weight loss peak in TGA analysis showed that 3.79% of overall weight loss occurred at 700 °C. These results indicated that the calcination process removed the surface capping molecules of black lemon peel extract. Good thermal stability was observed at annealing temperature of 500 °C with a weight loss of 53%.

To further ascertain the crystal phase of synthesized LP-ZnO NPs, Raman spectroscopic analysis was attained. In general, wurtzite ZnO NPs are expected to possess eight sets of corresponding optical phonon modes centered on the Brillouin zone (Γ) points as per the following equation:

$$\Gamma = 1A_1 + 2B_1 + 1E_1 + 2E_2 \quad (1)$$

where A_1 and E_1 are optical components of two polar branches that split into longitudinal optical (LO) and transversal optical (TO) components of varying frequencies associated with macroscopic electric fields accompanied by LO phonons. However, the observed E_2 modes are expected from nonpolar components, and low-frequency mode E_{2L} and high-frequency mode E_{2H} are obtained due to the presence of heavy Zn sublattice and only oxygen atoms, respectively [59]. A_1 , E_1 , and E_2 are active modes in infrared and Raman spectra. Meanwhile, the B_1 modes are generally known as silent modes as such modes are inactive in Raman spectra. A close perusal of Figure 7 shows a sharp peak characterized as E_2 (H) at 438 cm^{-1} corresponding to the Raman active optical phonon mode related to the wurtzite hexagonal phase of LP-ZnO NPs. The peak observed at 98 cm^{-1} was attributed to E_2 (LO), and the peak at 201 cm^{-1} was assigned to $2E_2$ (LO) after the second-order Raman spectrum. However, these peaks originated via E_2 (H)– E_2 (L) of the zone boundary phonons, as observed by the peak at 330 cm^{-1} . The peak at 387 cm^{-1} was attributed to A_1 (TO) modes of LP-ZnO NPs. In addition, the observed low-intensity peak at 558 cm^{-1} was assigned to E_1 (TO), and the relatively sharp peak intensity at 580 cm^{-1} was assigned to E_1

(LO) vibration modes. All our results from Raman data at different modes indicated that multiphoton resonances were present in the LP-ZnO NPs with a crystalline structure.

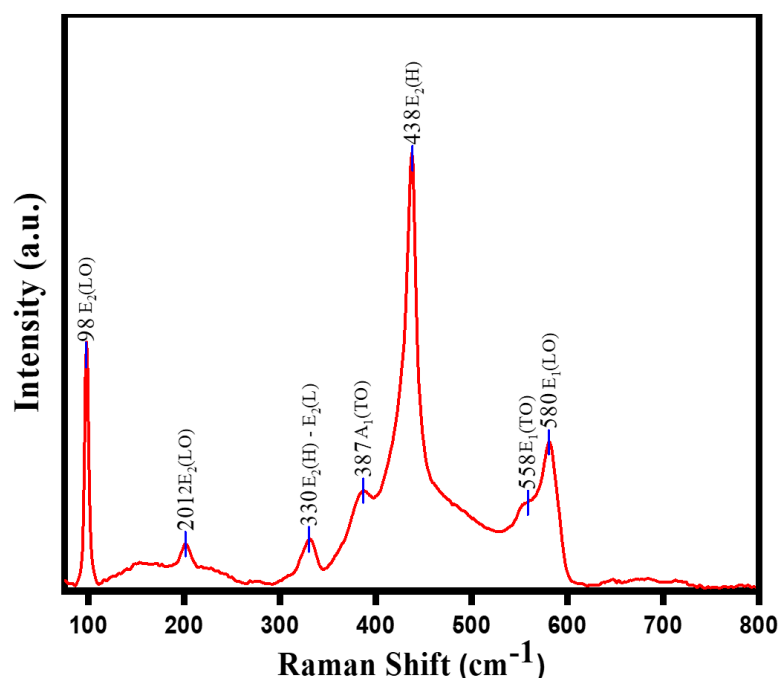


Figure 7. Raman spectra of LP-ZnO NPs.

The N_2 adsorption/desorption isotherm plot of LP-ZnO NPs is depicted in Figure 8a. The as-obtained isotherm for LP-ZnO NPs was type IV isotherm composed of H_3 hysteresis loop; the P/P_0 numerical values were found to be within the range of 0.8–0.95, corresponding to the presence of mesoporous texture of biosynthesized LP-ZnO NPs with slit-like pores. The observed loops were prominent at relatively higher pressure, which might be due to the pores within the interparticle spaces. In addition, the pore morphology, as deduced from the N_2 adsorption/desorption isotherm, was not apparent in the SEM images after the accumulation of spherical or nearly spherical LP-ZnO NPs in a rod-like pattern. The N_2 adsorption/desorption isotherm analysis was further validated for the pore size distribution using DFT analysis. Our results ascertained amorphous/crystalline heterostructure with slit-like microporous structures of higher specific surface area. Meanwhile, BET surface area of $24.543 \text{ m}^2/\text{g}$ with a volume of 0.037 cc/g and half pore width (Mode) of 13.845 \AA was attained, as depicted in Figure 8b.

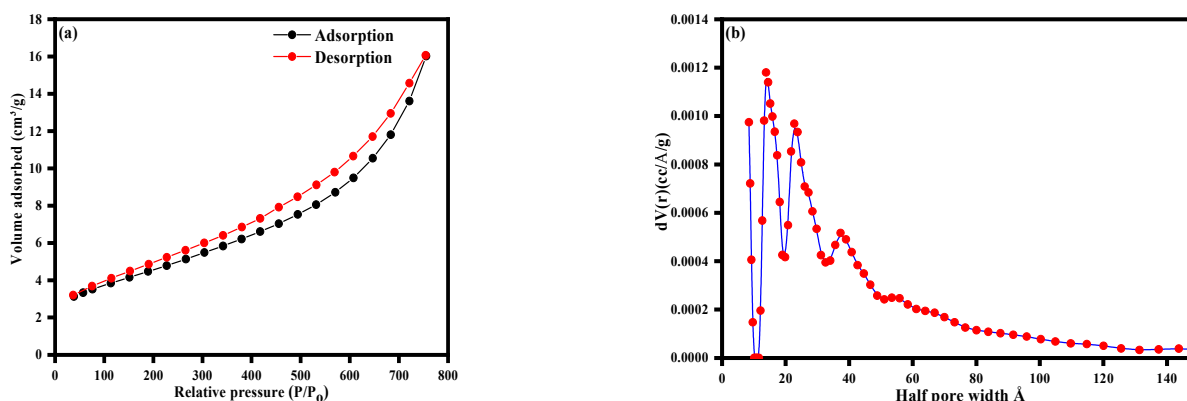


Figure 8. (a) Nitrogen adsorption/desorption isotherm plot and (b) micropore size distribution from the DFT model.

For LP-ZnO NPs, the SEM image showed numerous spherical and nearly spherical particles agglomerated and in rod-like patterns, as shown in Figure 9a–c. The formation of LP-ZnO NPs was further confirmed using EDX analysis, which revealed the presence of 78.23% zinc and 21.77% oxygen, as shown in Figure 9d, thus indicating the successful biosynthesis of LP-ZnO NPs in purified form. The presence of the C elemental signal could be due to the presence of surface capping agents on the surface of LP-ZnO NPs.

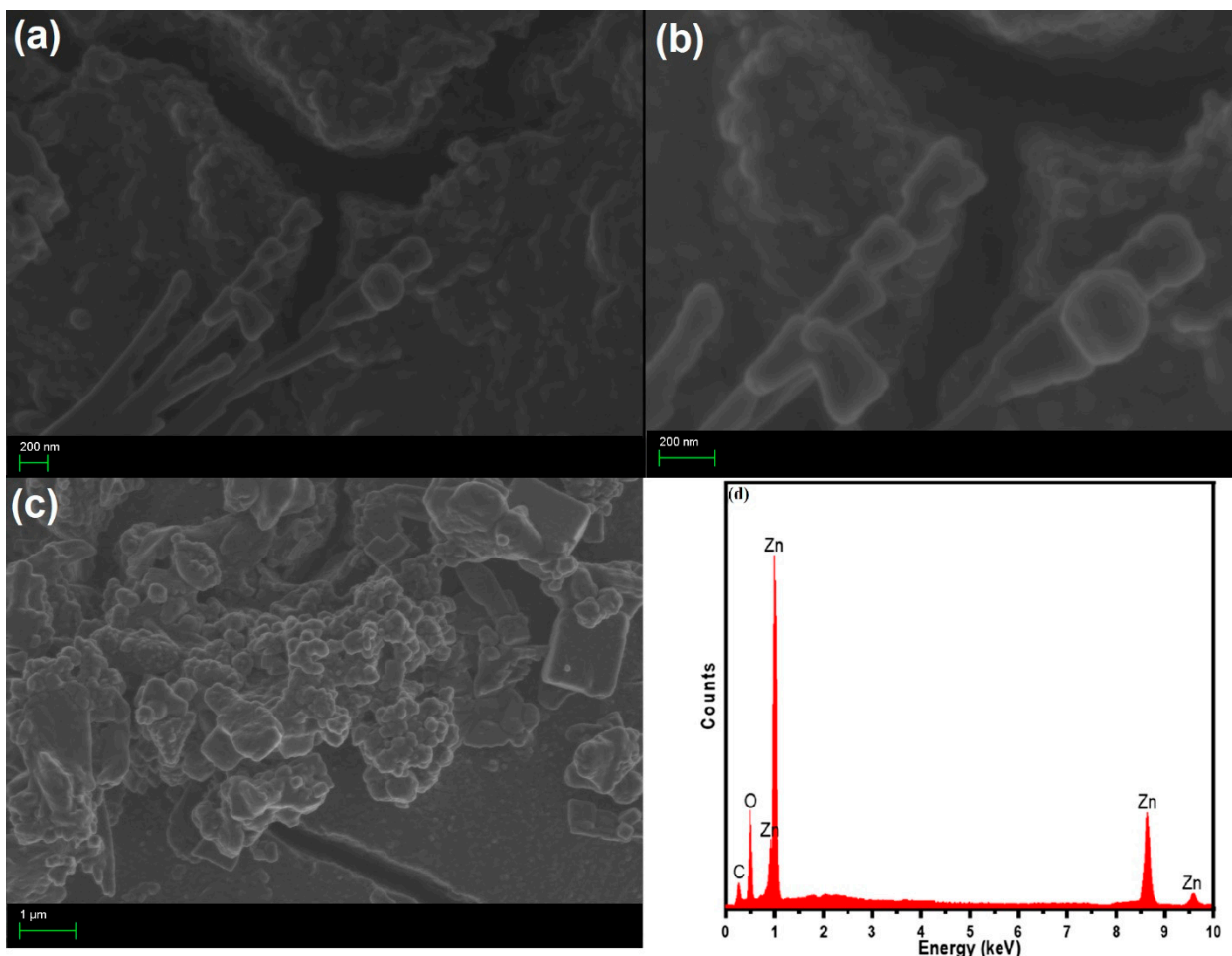


Figure 9. (a–c) SEM images and (d) EDX spectra of LP-ZnO NPs.

3.2. Photodegradation of Ciprofloxacin in the Presence of PL-ZnO NPs

Photocatalytic PL-ZnO NP mediated ciprofloxacin (CIP) degradation was ascertained in the presence of UV light, as depicted in Figure 10a. In general, UV light radiations alone are incapable of degradation or removal of CIP from their aqueous solution [60]. However, the degradation efficiency of CIP is comparatively much less under visible light irradiation in dark conditions than in the photocatalytic process [61]. We attained progressive photodegradation of CIP molecules in the presence of a catalyst (PL-ZnO NPs) at a peak maximum, i.e., 274 nm, along with two small peak intensities at ca. 320 and 332 nm. The complete diminishing of peak intensities ascertained the photodegradation of CIP within 160 min exposure time.

Meanwhile, the efficiency of degradation percentage of CIP molecules in their mixed solution was estimated from the relative intensity of the observed absorbance in UV–visible spectra. The decrease in relative absorbance reached approximately zero within 160 min exposure, revealing that the photocatalytic PL-ZnO NPs degraded CIP molecules in mixed solution by about 82%, as depicted in Figure 10b. Remarkably, the observed improvement in the photodegradation of CIP in the presence of a nanocatalyst (LP-ZnO NPs) under

UV light irradiation was attributed to the formation of hydroxyl radicals possessing a powerful oxidizing property. In addition, with the progression of the chemical reaction, the as-formed by-products under the influence of UV light irradiation might interact with the hydroxyl radicals in the adsorption sites on the surface of the nanocatalyst (LP-ZnO NPs). The observed gradual degradation/diminishing of peak intensities is visualized in Figure 10a,b.

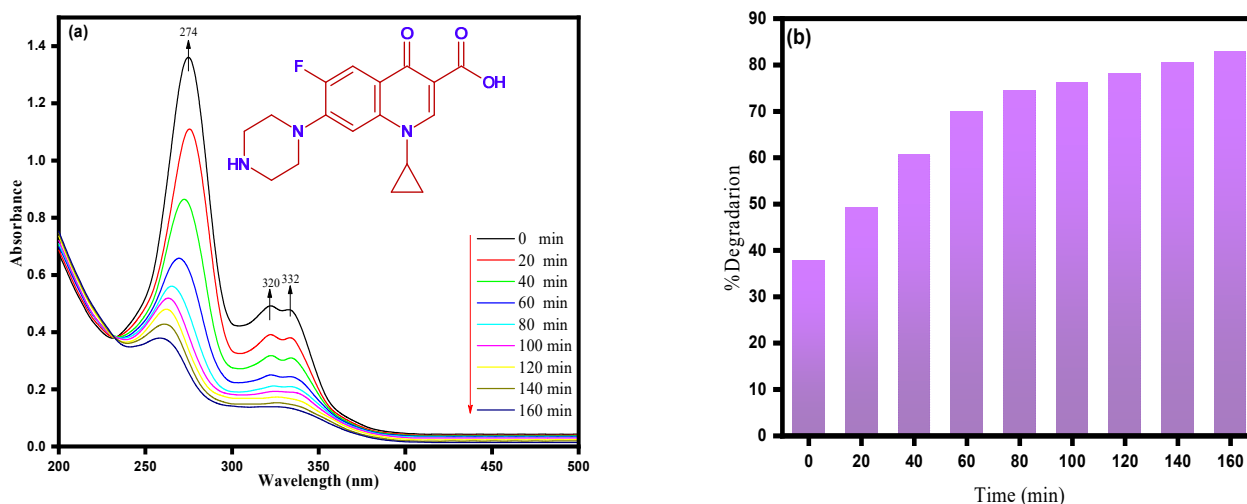


Figure 10. (a) Photocatalytic PL-ZnO NP mediated ciprofloxacin (CIP) degradation and (b) percentage degradation vs. time (min) of PL-ZnO NP mediated ciprofloxacin (CIP).

Catalytic dose degradation essay is an important parameter after determining the photoassisted degradation of pharmaceutical products [62]. The discoloration due to UV light irradiation of CIP molecules in the presence of a nanocatalyst (LP-ZnO) was determined by the Langmuir–Hinshelwood pseudo-first-order kinetics model [63]. Therefore, kinetic analysis at a different catalytic dose between 2 and 10 mg was accomplished by keeping a constant CIP concentration along with a constant UV light intensity. Meanwhile, a C_t/C_0 curve against time (min) was established to infer CIP photodegradation, as depicted in Figure 11a. However, we observed maximum photodegradation of CIP molecules at a comparatively higher catalytic dose, viz. 10 mg, most plausibly after generating maximum electron-hole pairs in light radiation.

Furthermore, an increase in the catalytic dose has the potential to occupy the existing active sites, and further accumulation and sedimentation in the reaction mixture will arrest the possible diffusions of photons. Another reason is the poorer penetration of photons into a comparatively higher concentrated mixture solution because of turbidity, thus leading to opacity. However, the scattering of light radiation can reduce the possible passage of irradiation in a mixture solution with a lower numerical degradation value. In the present study, we observed the optimum catalytic dose of comparatively higher concentration, i.e., 10 mg, as an efficient dose for photodegradation of CIP molecules.

The initial concentration effects of mixed CIP solution with a constant concentration of photocatalyst (LP-ZnO NPs) were investigated. The results are depicted in Figure 11b, which shows a plot of $\ln C_0/C_t$ against irradiation time (min) as per the Langmuir–Hinshelwood kinetic pseudo-first-order kinetic model. The optimization of pharmaceutical by-products, i.e., CIP molecules, was investigated in the range of 2×10^{-5} to 10×10^{-5} M at a constant dose of LP-ZnO NPs and maintained at basic pH (i.e., pH = 8) with an irradiation time of 160 min. However, a close glance at Figure 11b shows that an increase in the concentration of CIP molecules led to a decrease in photodegradation at a constant catalytic dose with an increase in time intervals up to 160 min irradiation in the presence of UV light radiation. The results of our study were obtained from the interaction of maximum possible binding sites in LP-ZnO NPs (fixed concentration) with increased CIP molecules

with enhanced photodegradation. In addition to catalytic poisoning, our photodegradation results emphasized the increased concentration of CIP molecules and the predominance of molecular interaction between active sites of LP-ZnO NPs and CIP molecules, which is a possible reason for observing higher (%) degradation at higher initial concentration of CIP molecules. In light radiation, at higher concentrations of CIP molecules, the generation of electron-hole pairs is enhanced in the presence of a constant catalytic dose.

Consequently, increased photodegradation efficiency was observed. In general, the process of photodegradation is behind reactive oxidation species (ROS), including the photogeneration of hydroxyl radicals ($\bullet\text{OH}$), hole pairs (h^+), superoxide anion radicals ($\text{O}_2^{\bullet-}$), and negatively charged electrons (e^-) [64]. As increased ROS with increased CIP molecules at a constant dose of LP-ZnO NP were observed in our study, we concluded that a comparatively higher concentration of CIP, i.e., 10×10^{-5} M, was the optimum concentration for photodegradation of CIP molecules in the presence of both photocatalyst LP-ZnO NPs and light radiation.

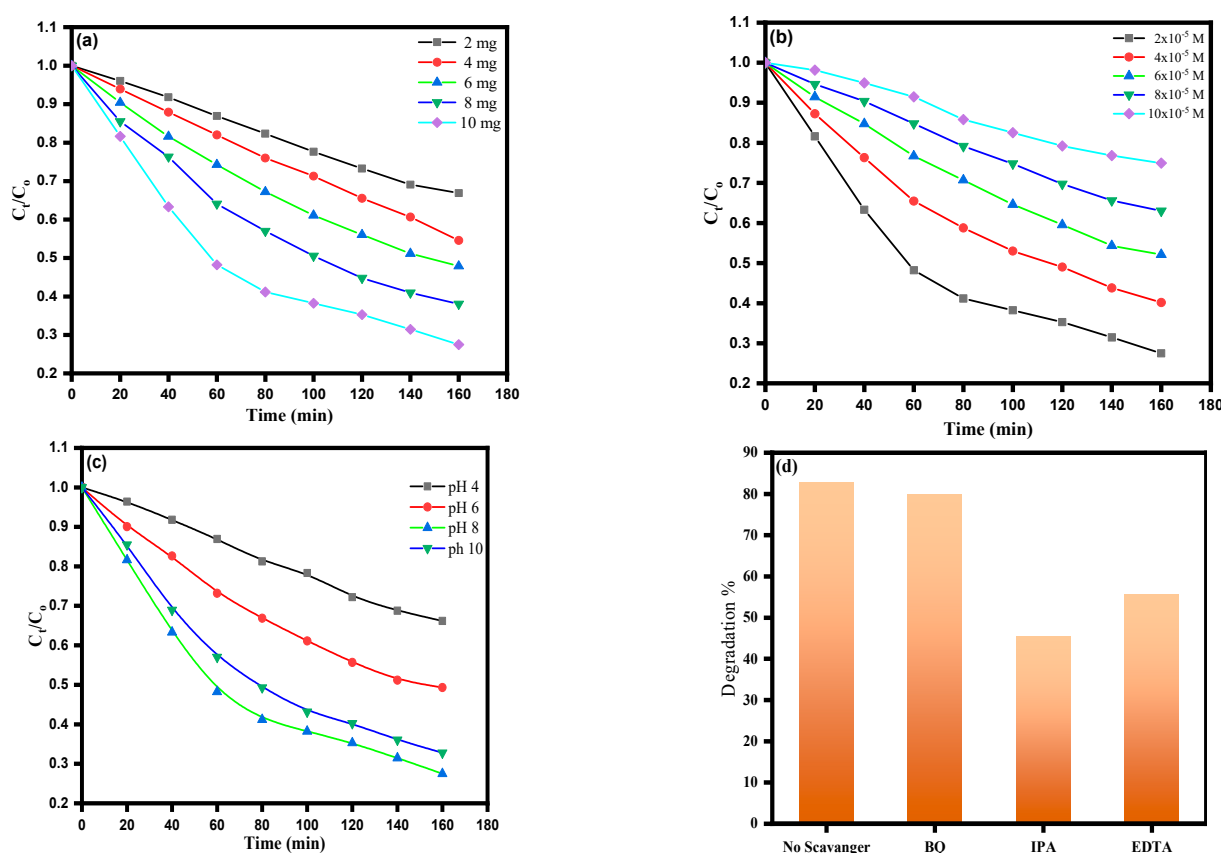


Figure 11. (a) Kinetic photodegradation of ciprofloxacin (CIP) at varying doses of nanocatalyst; (b) kinetic photodegradation at various initial concentrations of CIP molecules at a constant nanocatalyst dose; (c) pH-dependent kinetic photodegradation of ciprofloxacin (CIP) in the presence of a nanocatalyst (LP-ZnO); (d) effect of various scavengers on the photocatalytic degradation of ciprofloxacin in the presence of LP-ZnO NPs.

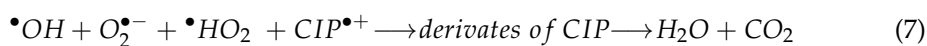
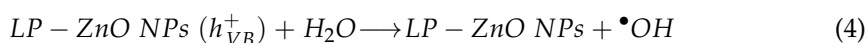
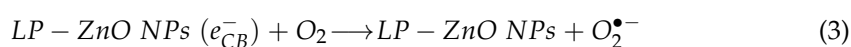
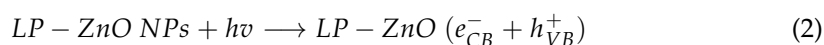
The pH analysis of catalytic photodegradation plays an important role in understanding the reaction conditions for the degradation of various organic dye molecules and pharmaceutical organic by-products as pollutants. We established a pH-dependent photodegradation method for CIP molecules with experimental conditions fixed at CIP = 2×10^{-5} M, LP-ZnO NPs = 10 mg, and temperature = 30 °C. Photodegradation was carried out at varying pH values in the range between pH 4 to 10. The results were plotted as per the Langmuir–Hinshelwood pseudo-first-order kinetic model, i.e., C_0/C_t against time (min), as depicted in Figure 11c. It is apparent from the plot that the maximum photodegradation of

LP-ZnO NP mediated CIP was attained with comparatively higher numerical values of pH, i.e., pH 8 and 10 (basic media), compared to pH 6, 4, and 2 (acidic media). The observed maximum photodegradation was believed to be due to the photogeneration of maximum hydroxyl ions in the presence of UV light. Furthermore, the hydroxyl ions generated upon reaction with positive holes (h^+) were changed into hydroxyl radicals ($\bullet OH$) with higher oxidation ability. Consequently, photodegradation of CIP molecules in basic media was enhanced. Similar results were perversely reported for CIP molecules in aromatic contaminants via ZnO NPs [65,66]. The presence of a photocatalyst has a significant effect on the photodegradation of CIP molecules in aqueous media. Depending on the pH of the solution, CIP molecules can exist in three forms: cationic, anionic, and zwitter ions. However, the deprotonation or polarization of charge onto the surface of the photocatalyst is too dependent on the pH of the solution. Thus, the possible molecular interactions among CIP, water molecules, and photogenerated radicals make a critical contribution toward photocatalytic degradation. In addition, the charge on the surface of the photocatalyst is more protonated at lower pH, and the reverse is also true, i.e., deprotonation usually occurs at comparatively higher pH situations [67]. At lower numerical values between pH 6 and 2, the observed photodegradation of LP-ZnO mediated CIP molecules was impeded with higher concentration of protons. These protons had much more affinity toward hydroxyl anion and led to the disintegration of hydroxyl radical formation with impeded photodegradation of LP-ZnO mediated CIP molecules. Meanwhile, at lower numerical values of pH, i.e., in acidic media, both the surface charge of the photocatalyst and CIP molecules tended to predominate negatively charged species, resulting in repulsion and reducing the degradation efficacy of the photocatalytic process. Our pH-dependent photocatalysis of CIP molecules in the presence of LP-ZnO NPs facilitated maximum photocatalysis of CIP molecules in an aqueous mixed media in basic media i.e., at higher numerical pH values, such as at pH 8 and 10.

The active species of the photocatalytic process was detected by a trapping experiment. Figure 11d reveals the degradation rate of ciprofloxacin after three kinds of free radical scavengers, namely, BQ, IPA, and EDTA, were added to the photocatalytic degradation system. BQ, IPA, and EDTA were applied to capture $\bullet O_2^-$, $\bullet OH$, and h^+ , respectively. The degradation rate decreased to a certain degree with the addition of BQ, indicating that $\bullet O_2^-$ had a specific effect on ciprofloxacin degradation. The degradation efficiency of ciprofloxacin was also reduced with addition of EDTA, which showed that h^+ had some role in the reaction process. When IPA was added as the scavenger of $\bullet OH$, the degradation efficiency of ciprofloxacin was significantly reduced, indicating the primary effect of $\bullet OH$ in the photodegradation of ciprofloxacin. We can conclude from these observations that $\bullet OH$ is very important in the photocatalytic degradation of ciprofloxacin with the sequence $\bullet OH > h^+ > \bullet O_2^-$.

3.3. Proposed Possible Mechanism behind Photocatalytic Degradation of CIP

The photodegradation mechanism of CIP molecules via LP-ZnO mediated catalysis follows the generation of reactive oxidative species, such as hydroxyl radicals, holes, electrons, and superoxides, in a photocatalytic reaction. Therefore, the mechanism of a reaction involving photocatalysis of pharmaceutical by-products of CIP molecules can be assumed as follows:



LP-ZnO NPs can be regarded as a semiconductor photocatalyst that possesses an ability to undergo photoexcitation in the presence of light illumination greater than that of the bandgap. Meanwhile, e^- excitation from the valence band (VB) to the conduction band (CB) results in vacant h^+ holes in the VB. In our study, the photoirradiated LP-ZnO NPs in the presence of UV light generated e^- in the CB, and respective h^+ was formed in the VB as per Equation (2). The e^- of CB reacted with oxygen molecules to generate $\bullet O_2^-$ free radicals, which, on further reaction with proton, gave $\bullet HO_2$ as per Equations (4) and (5). However, as per Equation (4), the h^+ holes of VB reacted with LP-ZnO NPs in water to generate hydroxyl-free radicals (OH^\bullet). Overall, the ROS were photogenerated in a catalytic reaction, which facilitated the possible degradation of CIP molecules, as shown in a stepwise equation in Equations (6) and (7), in a photocatalyzed reduction process. The process is presented systematically in Figure 12.

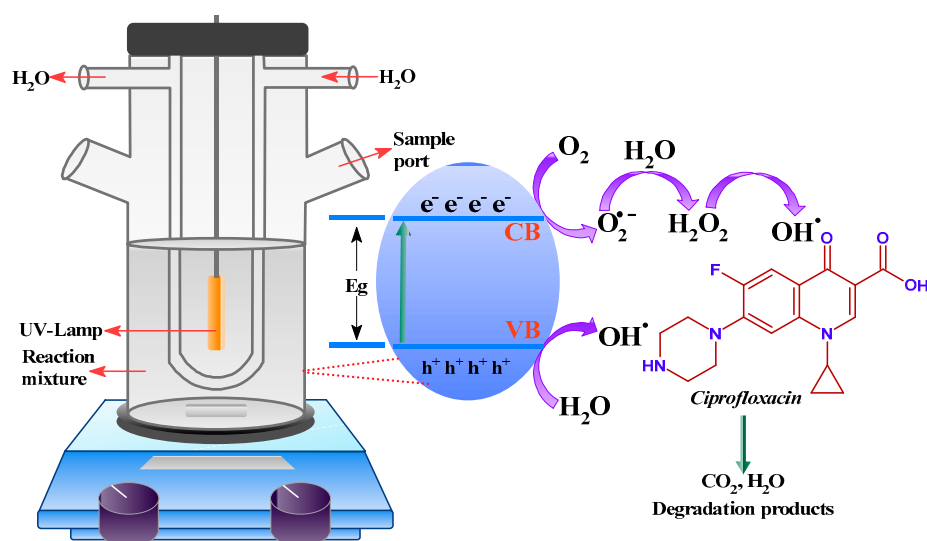


Figure 12. Schematic representation of photocatalytic degradation and mechanism after photodegradation via a catalyst (LP-ZnO NPs).

4. Conclusions

A facile green precipitation synthesis method was introduced to prepare stable LP-ZnO NPs. Various methods were used to characterize the biogenic LP-ZnO NPs. XRD analysis ascertained the successful synthesis of LP-ZnO NPs with an average crystalline size of 20 nm. The synthesized nanoparticles showed lower binding energy values, further confirming their use as photocatalysts for their excellent electron transition capabilities as per UV-visible DRS analysis. The surface morphology with spherical or nearly spherical LP-ZnO NPs with rod-like structure was confirmed from PL and SEM analyses. Furthermore, the biogenesis of LP-ZnO NPs was supported by several peak shifts observed in FTIR analysis. The surface morphology with crystalline structure of LP-ZnO NPs was also deduced by observing different modes of multiphoton resonance of Raman spectra. In addition, the as-synthesized LP-ZnO NPs were thermally stable as demonstrated by TGA analysis. In response to UV light irradiation, LP-ZnO NPs exhibited strong photocatalytic activity toward ciprofloxacin and retained more than 90% ciprofloxacin degradation within 160 min. The results of the free radical capture indicated that the main active substance was $\bullet OH$, while $O_2^{\bullet-}$ and h^+ were almost not produced in the degradation of ciprofloxacin. The present work may provide a strategy for preparing efficient UV light photocatalysts. Meanwhile, the pH of the solution played a crucial role in the degradation of antibiotics, and high photocatalytic activity of LP-ZnO NPs was observed at pH 8. The lemon peel extract utilized in the preparation of ZnO NPs is inexpensive, easily available, safe, eco-friendly, and not harmful to our ecosystem.

Author Contributions: Conceptualization, M.A.M., M.R.K., M.G.B. and A.N.; data curation, M.G.B., K.A.A. and E.Y.D.; formal analysis, M.A.M., M.G.B. and A.N.; investigation, M.G.B., K.A.A. and E.Y.D.; methodology, M.A.M., M.R.K., M.G.B. and A.N.; project administration, M.R.K.; software, K.A.A. and E.Y.D.; supervision, M.A.M. and E.Y.D.; validation, M.A.M., K.A.A. and A.N.; writing—original draft, M.A.M., M.R.K., M.G.B. and A.N.; writing—review and editing, M.A.M., M.R.K., M.G.B., A.N., K.A.A. and E.Y.D. All authors have read and agreed to the published version of the manuscript.

Funding: Institutional Fund Projects under grant number (IFPIP: 944-130-1442) by the Ministry of Education and King Abdulaziz University, DSR, Jeddah, Saudi Arabia.

Data Availability Statement: All relevant data are within the paper.

Acknowledgments: This research work was funded by the Institutional Fund Projects under grant number (IFPIP: 944-130-1442). Therefore, authors gratefully acknowledge technical and financial support from the Ministry of Education and King Abdulaziz University, DSR, Jeddah, Saudi Arabia.

Conflicts of Interest: The authors declare no conflict of interest.

References

1. Pan, S.; Goudoulas, T.B.; Jeevanandam, J.; Tan, K.X.; Chowdhury, S.; Danquah, M.K. Therapeutic Applications of Metal and Metal-Oxide Nanoparticles: Dermato-Cosmetic Perspectives. *Front. Bioeng. Biotechnol.* **2021**, *9*, 724499. [[CrossRef](#)] [[PubMed](#)]
2. Chavali, M.S.; Nikolova, M.P. Metal oxide nanoparticles and their applications in nanotechnology. *SN Appl. Sci.* **2019**, *1*, 607. [[CrossRef](#)]
3. Nikolova, M.P.; Chavali, M.S. Metal oxide nanoparticles as biomedical materials. *Biomimetics* **2020**, *5*, 27. [[CrossRef](#)] [[PubMed](#)]
4. Yaqoob, A.A.; Ahmad, H.; Parveen, T.; Ahmad, A.; Oves, M.; Ismail, I.M.; Qari, H.A.; Umar, K.; Mohamad Ibrahim, M.N. Recent advances in metal decorated nanomaterials and their various biological applications: A review. *Front. Chem.* **2020**, *8*, 341. [[CrossRef](#)]
5. Kelly, K.L.; Coronado, E.; Zhao, L.L.; Schatz, G.C. The optical properties of metal nanoparticles: The influence of size, shape, and dielectric environment. *J. Phys. Chem. B* **2003**, *107*, 668–677. [[CrossRef](#)]
6. Kamli, M.R.; Malik, M.A.; Lone, S.A.; Sabir, J.S.; Mattar, E.H.; Ahmad, A. Beta vulgaris Assisted Fabrication of Novel Ag-Cu Bimetallic Nanoparticles for Growth Inhibition and Virulence in *Candida albicans*. *Pharmaceutics* **2021**, *13*, 1957. [[CrossRef](#)]
7. Kamli, M.R.; Malik, M.A.; Srivastava, V.; Sabir, J.S.; Mattar, E.H.; Ahmad, A. Biogenic ZnO Nanoparticles Synthesized from *Origanum vulgare* Abrogates Quorum Sensing and Biofilm Formation in Opportunistic Pathogen *Chromobacterium violaceum*. *Pharmaceutics* **2021**, *13*, 1743. [[CrossRef](#)]
8. Sharma, D.; Kanchi, S.; Bisetty, K. Biogenic synthesis of nanoparticles: A review. *Arab. J. Chem.* **2019**, *12*, 3576–3600. [[CrossRef](#)]
9. Siddiquee, M.A.; ud din Parray, M.; Kamli, M.R.; Malik, M.A.; Mehdi, S.H.; Imtiyaz, K.; Rizvi, M.M.A.; Rajor, H.K.; Patel, R. Biogenic synthesis, in-vitro cytotoxicity, esterase activity and interaction studies of copper oxide nanoparticles with lysozyme. *J. Mater. Res. Technol.* **2021**, *13*, 2066–2077. [[CrossRef](#)]
10. Kamli, M.R.; Srivastava, V.; Hajrah, N.H.; Sabir, J.S.; Hakeem, K.R.; Ahmad, A.; Malik, M.A. Facile bio-fabrication of Ag-Cu-Co trimetallic nanoparticles and its fungicidal activity against *Candida auris*. *J. Fungi* **2021**, *7*, 62. [[CrossRef](#)]
11. Malik, M.A.; Alshehri, A.A.; Patel, R. Facile one-pot green synthesis of Ag-Fe bimetallic nanoparticles and their catalytic capability for 4-nitrophenol reduction. *J. Mater. Res. Technol.* **2021**, *12*, 455–470. [[CrossRef](#)]
12. Alshehri, A.A.; Malik, M.A. Phytomediated photo-induced green synthesis of silver nanoparticles using *Matricaria chamomilla* L. and its catalytic activity against rhodamine B. *Biomolecules* **2020**, *10*, 1604. [[CrossRef](#)] [[PubMed](#)]
13. Borysiewicz, M.A. ZnO as a functional material, a review. *Crystals* **2019**, *9*, 505. [[CrossRef](#)]
14. Mishra, Y.K.; Adelung, R. ZnO tetrapod materials for functional applications. *Mater. Today* **2018**, *21*, 631–651. [[CrossRef](#)]
15. Ortiz-Casas, B.; Galdámez-Martínez, A.; Gutiérrez-Flores, J.; Ibañez, A.B.; Panda, P.K.; Santana, G.; de la Vega, H.A.; Suar, M.; Rodelo, C.G.; Kaushik, A. Bio-Acceptable 0D and 1D ZnO nanostructures for cancer diagnostics and treatment. *Mater. Today* **2021**, *50*, 533–569. [[CrossRef](#)]
16. Ali, M.; Ahmed, T.; Wu, W.; Hossain, A.; Hafeez, R.; Islam Masum, M.; Wang, Y.; An, Q.; Sun, G.; Li, B. Advancements in plant and microbe-based synthesis of metallic nanoparticles and their antimicrobial activity against plant pathogens. *Nanomaterials* **2020**, *10*, 1146. [[CrossRef](#)]
17. Kamli, M.R.; Srivastava, V.; Hajrah, N.H.; Sabir, J.S.; Ali, A.; Malik, M.A.; Ahmad, A. Phytogenic Fabrication of Ag-Fe Bimetallic Nanoparticles for Cell Cycle Arrest and Apoptosis Signaling Pathways in *Candida auris* by Generating Oxidative Stress. *Antioxidants* **2021**, *10*, 182. [[CrossRef](#)]
18. Mukherjee, A.; Sarkar, D.; Sasmal, S. A review of green synthesis of metal nanoparticles using algae. *Front. Microbiol.* **2021**, *12*, 693899. [[CrossRef](#)]
19. Das, R.K.; Pachapur, V.L.; Lonappan, L.; Naghdi, M.; Pulicharla, R.; Maiti, S.; Cledon, M.; Dalila, L.M.A.; Sarma, S.J.; Brar, S.K. Biological synthesis of metallic nanoparticles: Plants, animals and microbial aspects. *Nanotechnol. Environ. Eng.* **2017**, *2*, 18. [[CrossRef](#)]

20. He, Q.; Liu, J.; Huang, C.; Wu, W. Synthesis and characterization of a silver incorporated magnetic nanocomposite with enhanced antibacterial activity. *Sci. Adv. Mater.* **2014**, *6*, 366–376. [[CrossRef](#)]
21. Khetan, S.K.; Collins, T.J. Human pharmaceuticals in the aquatic environment: A challenge to green chemistry. *Chem. Rev.* **2007**, *107*, 2319–2364. [[CrossRef](#)] [[PubMed](#)]
22. Ma, D.; Wu, T.; Zhang, J.; Lin, M.; Mai, W.; Tan, S.; Xue, W.; Cai, X. Supramolecular hydrogels sustained release triclosan with controlled antibacterial activity and limited cytotoxicity. *Sci. Adv. Mater.* **2013**, *5*, 1400–1409. [[CrossRef](#)]
23. Rokesh, K.; Sakar, M.; Do, T.-O. Emerging hybrid nanocomposite photocatalysts for the degradation of antibiotics: Insights into their designs and mechanisms. *Nanomaterials* **2021**, *11*, 572. [[CrossRef](#)] [[PubMed](#)]
24. Church, N.A.; McKillip, J.L. Antibiotic resistance crisis: Challenges and imperatives. *Biologia* **2021**, *76*, 1535–1550. [[CrossRef](#)]
25. Nasuhoglu, D.; Rodayan, A.; Berk, D.; Yargeau, V. Removal of the antibiotic levofloxacin (LEVO) in water by ozonation and TiO₂ photocatalysis. *Chem. Eng. J.* **2012**, *189*, 41–48. [[CrossRef](#)]
26. Talebi Bezin Abadi, A.; Rizvanov, A.A.; Haertlé, T.; Blatt, N.L. World Health Organization report: Current crisis of antibiotic resistance. *BioNanoScience* **2019**, *9*, 778–788. [[CrossRef](#)]
27. Akbari, M.Z.; Xu, Y.; Lu, Z.; Peng, L. Review of antibiotics treatment by advance oxidation processes. *Environ. Adv.* **2021**, *5*, 100111. [[CrossRef](#)]
28. Hassan, M.; Zhu, G.; Lu, Y.-z.; AL-Falahi, A.H.; Yuan, L.; Huang, S.; Wan, Z. Removal of antibiotics from wastewater and its problematic effects on microbial communities by bioelectrochemical technology: Current knowledge and future perspectives. *Environ. Eng. Res.* **2021**, *26*, 16–30. [[CrossRef](#)]
29. Hiller, C.; Hübner, U.; Fajnorova, S.; Schwartz, T.; Drewes, J. Antibiotic microbial resistance (AMR) removal efficiencies by conventional and advanced wastewater treatment processes: A review. *Sci. Total Environ.* **2019**, *685*, 596–608. [[CrossRef](#)]
30. Huang, A.; Yan, M.; Lin, J.; Xu, L.; Gong, H.; Gong, H. A review of processes for removing antibiotics from breeding wastewater. *Int. J. Environ. Res. Public Health* **2021**, *18*, 4909. [[CrossRef](#)]
31. Huang, Y.-H.; Liu, Y.; Du, P.-P.; Zeng, L.-J.; Mo, C.-H.; Li, Y.-W.; Lü, H.; Cai, Q.-Y. Occurrence and distribution of antibiotics and antibiotic resistant genes in water and sediments of urban rivers with black-odor water in Guangzhou, South China. *Sci. Total Environ.* **2019**, *670*, 170–180. [[CrossRef](#)]
32. Reis, A.C.; Kolvenbach, B.A.; Nunes, O.C.; Corvini, P.F. Biodegradation of antibiotics: The new resistance determinants—part I. *New Biotechnol.* **2020**, *54*, 34–51. [[CrossRef](#)]
33. Zhi, D.; Yang, D.; Zheng, Y.; Yang, Y.; He, Y.; Luo, L.; Zhou, Y. Current progress in the adsorption, transport and biodegradation of antibiotics in soil. *J. Environ. Manag.* **2019**, *251*, 109598. [[CrossRef](#)]
34. Brillas, E. A review on the photoelectro-Fenton process as efficient electrochemical advanced oxidation for wastewater remediation. Treatment with UV light, sunlight, and coupling with conventional and other photo-assisted advanced technologies. *Chemosphere* **2020**, *250*, 126198. [[CrossRef](#)]
35. Cuerda-Correa, E.M.; Alexandre-Franco, M.F.; Fernández-González, C. Advanced oxidation processes for the removal of antibiotics from water. An overview. *Water* **2019**, *12*, 102. [[CrossRef](#)]
36. Giwa, A.; Yusuf, A.; Balogun, H.A.; Sambudi, N.S.; Bilad, M.R.; Adeyemi, I.; Chakraborty, S.; Curcio, S. Recent advances in advanced oxidation processes for removal of contaminants from water: A comprehensive review. *Process Saf. Environ. Prot.* **2021**, *146*, 220–256. [[CrossRef](#)]
37. Lops, C.; Ancona, A.; Di Cesare, K.; Dumontel, B.; Garino, N.; Canavese, G.; Hernández, S.; Cauda, V. Sonophotocatalytic degradation mechanisms of Rhodamine B dye via radicals generation by micro-and nanoparticles of ZnO. *Appl. Catal. B Environ.* **2019**, *243*, 629–640. [[CrossRef](#)]
38. Gowthambabu, V.; Balamurugan, A.; Satheeshkumar, S.; Kanmani, S. ZnO nanoparticles as efficient sunlight driven photocatalyst prepared by solution combustion method involved lime juice as biofuel. *Spectrochim. Acta Part A Mol. Biomol. Spectrosc.* **2021**, *258*, 119857. [[CrossRef](#)]
39. Muruganandham, M.; Zhang, Y.; Suri, R.; Lee, G.-J.; Chen, P.-K.; Hsieh, S.-H.; Sillanpää, M.; Wu, J.J. Environmental applications of ZnO materials. *J. Nanosci. Nanotechnol.* **2015**, *15*, 6900–6913. [[CrossRef](#)]
40. Jayachandran, A.; Aswathy, T.R.; Nair, A.S. Green synthesis and characterization of zinc oxide nanoparticles using Cayratia pedata leaf extract. *Biochem. Biophys. Rep.* **2021**, *26*, 100995. [[CrossRef](#)]
41. Jeevanandam, J.; Chan, Y.S.; Danquah, M.K. Biosynthesis of Metal and Metal Oxide Nanoparticles. *ChemBioEng Rev.* **2016**, *3*, 55–67. [[CrossRef](#)]
42. Sahoo, S.K.; Panigrahi, G.K.; Sahoo, A.; Pradhan, A.K.; Dalbehera, A. Bio-hydrothermal synthesis of ZnO–ZnFe₂O₄ nanoparticles using Psidium guajava leaf extract: Role in waste water remediation and plant immunity. *J. Clean. Prod.* **2021**, *318*, 128522. [[CrossRef](#)]
43. Alshehri, A.A.; Malik, M.A. Biogenic fabrication of ZnO nanoparticles using Trigonella foenum-graecum (Fenugreek) for proficient photocatalytic degradation of methylene blue under UV irradiation. *J. Mater. Sci. Mater. Electron.* **2019**, *30*, 16156–16173. [[CrossRef](#)]
44. Abomuti, M.A.; Danish, E.Y.; Firoz, A.; Hasan, N.; Malik, M.A. Green Synthesis of Zinc Oxide Nanoparticles Using Salvia officinalis Leaf Extract and Their Photocatalytic and Antifungal Activities. *Biology* **2021**, *10*, 1075.

45. Rauf, M.A.; Owais, M.; Rajpoot, R.; Ahmad, F.; Khan, N.; Zubair, S. Biomimetically synthesized ZnO nanoparticles attain potent antibacterial activity against less susceptible *S. aureus* skin infection in experimental animals. *RSC Adv.* **2017**, *7*, 36361–36373. [[CrossRef](#)]
46. Nagarajan, S.; Arumugam Kuppusamy, K. Extracellular synthesis of zinc oxide nanoparticle using seaweeds of gulf of Mannar, India. *J. Nanobiotechnology* **2013**, *11*, 39. [[CrossRef](#)]
47. Samanta, P.; Patra, S.; Ghosh, A.; Chaudhuri, P.R. Visible emission from ZnO nano-rods synthesized by a simple wet chemical method. *Int. J. Nanosci. Nanotechnol.* **2009**, *1*, 81–90.
48. Zhang, R.; Yin, P.-G.; Wang, N.; Guo, L. Photoluminescence and Raman scattering of ZnO nano-rods. *Solid State Sci.* **2009**, *11*, 865–869. [[CrossRef](#)]
49. Willander, M.; Nur, O.; Sadaf, J.R.; Qadir, M.I.; Zaman, S.; Zainelabdin, A.; Bano, N.; Hussain, I. Luminescence from zinc oxide nanostructures and polymers and their hybrid devices. *Materials* **2010**, *3*, 2643–2667.
50. Bindu, P.; Thomas, S. Estimation of lattice strain in ZnO nanoparticles: X-ray peak profile analysis. *J. Theor. Appl. Phys.* **2014**, *8*, 123–134. [[CrossRef](#)]
51. Arslanoglu, H.; Altundogan, H.S.; Tumen, F. Preparation of cation exchanger from lemon and sorption of divalent heavy metals. *Bioresour. Technol.* **2008**, *99*, 2699–2705. [[CrossRef](#)]
52. Berezin, K.; Likhter, A.; Shagautdinova, I.; Chernavina, M.; Novoselova, A. FT-IR and DFT study of lemon peel. In Proceedings of the Saratov Fall Meeting 2016: Optical Technologies in Biophysics and Medicine XVIII, Saratov, Russia, 27–30 September 2016; pp. 116–123.
53. Al-Qaisi, M.Q.; Faisal, L.; Al-Sharif, Z.T.; Al-Sharif, T.A. Possibility of utilizing from lemon peel as a sorbent in removing of contaminant such as copper ions from simulated aqueous solution. *Int. J. Civ. Eng. Technol.* **2018**, *9*, 571–579.
54. Villen-Guzman, M.; Cerrillo-Gonzalez, M.d.M.; Paz-Garcia, J.; Rodriguez-Maroto, J.M.; Arhoun, B. Valorization of lemon peel waste as biosorbent for the simultaneous removal of nickel and cadmium from industrial effluents. *Environ. Technol. Innov.* **2021**, *21*, 101380. [[CrossRef](#)]
55. Santhoshkumar, J.; Kumar, S.V.; Rajeshkumar, S. Synthesis of zinc oxide nanoparticles using plant leaf extract against urinary tract infection pathogen. *Resour.-Effic. Technol.* **2017**, *3*, 459–465. [[CrossRef](#)]
56. Viswanathan, K.; Kim, I.; Kasi, G.; Sadeghi, K.; Thanakkasaranee, S.; Seo, J. Facile approach to enhance the antibacterial activity of ZnO nanoparticles. *Adv. Appl. Ceram.* **2020**, *119*, 414–422. [[CrossRef](#)]
57. Faisal, S.; Jan, H.; Shah, S.A.; Shah, S.; Khan, A.; Akbar, M.T.; Rizwan, M.; Jan, F.; Wajidullah; Akhtar, N. Green synthesis of zinc oxide (ZnO) nanoparticles using aqueous fruit extracts of *Myristica fragrans*: Their characterizations and biological and environmental applications. *ACS Omega* **2021**, *6*, 9709–9722. [[CrossRef](#)]
58. Nimbalkar, A.R.; Patil, M.G. Synthesis of ZnO thin film by sol-gel spin coating technique for H₂S gas sensing application. *Phys. B Condens. Matter* **2017**, *527*, 7–15.
59. Xu, C.; Sun, X.; Zhang, X.; Ke, L.; Chua, S. Photoluminescent properties of copper-doped zinc oxide nanowires. *Nanotechnology* **2004**, *15*, 856. [[CrossRef](#)]
60. Taie, M.; Fadaei, A.; Sadeghi, M.; Hemati, S.; Mardani, G. Comparison of the efficiency of ultraviolet/zinc oxide (UV/ZnO) and ozone/zinc oxide (O₃/ZnO) techniques as advanced oxidation processes in the removal of trimethoprim from aqueous solutions. *Int. J. Chem. Eng.* **2021**, *2021*, 9640918.
61. Wolski, L.; Grzelak, K.; Muńko, M.; Frankowski, M.; Grzyb, T.; Nowaczyk, G. Insight into photocatalytic degradation of Ciprofloxacin over CeO₂/ZnO nanocomposites: Unravelling the synergy between the metal oxides and analysis of reaction pathways. *Appl. Surf. Sci.* **2021**, *563*, 150338. [[CrossRef](#)]
62. Trawiński, J.; Skibiński, R. Studies on photodegradation process of psychotropic drugs: A review. *Environ. Sci. Pollut. Res.* **2017**, *24*, 1152–1199. [[CrossRef](#)]
63. Hassan, S.S.; El Azab, W.I.; Ali, H.R.; Mansour, M.S. Green synthesis and characterization of ZnO nanoparticles for photocatalytic degradation of anthracene. *Adv. Nat. Sci. Nanosci. Nanotechnol.* **2015**, *6*, 045012. [[CrossRef](#)]
64. Nosaka, Y.; Nosaka, A.Y. Generation and detection of reactive oxygen species in photocatalysis. *Chem. Rev.* **2017**, *117*, 11302–11336. [[CrossRef](#)]
65. Hariharan, C. Photocatalytic degradation of organic contaminants in water by ZnO nanoparticles: Revisited. *Appl. Catal. A Gen.* **2006**, *304*, 55–61. [[CrossRef](#)]
66. El-Kemary, M.; El-Shamy, H.; El-Mehasseb, I. Photocatalytic degradation of ciprofloxacin drug in water using ZnO nanoparticles. *J. Lumin.* **2010**, *130*, 2327–2331. [[CrossRef](#)]
67. Gad-Allah, T.A.; Ali, M.E.; Badawy, M.I. Photocatalytic oxidation of Ciprofloxacin under simulated sunlight. *J. Hazard. Mater.* **2011**, *186*, 751–755. [[CrossRef](#)]